Classification: biological sciences; plant biology, cell biology,

Actin-dependent cellular occupancy of the vacuole determines auxin-induced growth repression

David Scheuring[a], Christian Löfke[a], Falco Krüger[b], Maike Kittelmann[c], Ahmed Eisa[a], Louise Hughes[c], Richard Smith[d], Chris Hawes[c], Karin Schumacher[b], Jürgen Kleine-Vehn[a,1]

[a]Department of Applied Genetics and Cell Biology, University of Natural Resources and Life Sciences (BOKU), 1190 Vienna, Austria; [b]Center for Organismal Studies (COS), University of Heidelberg, 69120 Heidelberg, Germany; [c]Department of Biological and Medical Sciences, Oxford Brookes University, Oxford OX3 0BP, United Kingdom ; [d]Max Planck Institute for Plant Breeding Research, 50829 Köln, Germany

[1]To whom correspondence should be addressed. Email: juergen.kleine-vehn@boku.ac.at

Corresponding author: Jürgen Kleine-Vehn
Department of Applied Genetics and Cell Biology
University of Natural Resources and Life Sciences (BOKU)
Muthgasse 18
1190 Vienna, Austria
Phone: +43-1-47654-6719
Email: juergen.kleine-vehn@boku.ac.at

Key words:

Auxin, vacuole, actin cytoskeleton, cell growth

The cytoskeleton is an early attribute of cellular life and its main components are composed of conserved proteins (Fletcher and Mullins, 2010). The actin cytoskeleton has a direct impact on cell size control in animal cells (Fletcher and Mullins, 2010; Faix et al., 1996), but its mechanistic contribution to cellular growth in plants remains largely elusive. Here, we reveal a role of actin in cell size regulation in plants. The actin cytoskeleton shows proximity to vacuoles, and the phytohormone auxin not only controls the organisation of actin filaments, but also impacts on vacuolar morphogenesis in an actin-dependent manner. Pharmacological and genetic interference with the actin-myosin system abolishes the auxin effect on vacuoles and thus disrupts its negative influence on cellular growth. SEM-based 3D nanometre resolution imaging of the vacuoles revealed that auxin controls the constriction and luminal size of the vacuole. We show that this actin-dependent mechanism controls the relative cellular occupancy of the vacuole, thus proposing an unanticipated mechanism for cytosol homeostasis during cellular growth.

Significance Statement:

Cell size control is fundamentally different in animals and plants. The actin cytoskeleton has a direct impact on cell size control in animals, but its mechanistic contribution to cellular growth in plants remains largely elusive. Here, we reveal that actin is utilized in a plant specific growth mechanism by controlling the volume of the largest plant organelle - the vacuole. Actin is required for the auxin-dependent convolution and de-convolution of the vacuole, steering the cellular occupancy of this organelle. This indirectly impacts on cytosol size and presumably allows plant cells to grow without alterations in cytosolic content. These findings could lead to a better understanding why plant cells are able to expand faster than vacuole-lacking animal cells.

/body

Actin filaments and its myosin motor proteins control a multitude of diverse cellular processes in animal cells, such as muscle contraction or cell motility, as well as vesicle and organelle movements (1). Actin has a strong impact on cellular shape regulation in animals and its impact on cell size is thus self-evident (2). In contrast to animals, plant cells are sheathed by shape-giving cell walls, rendering them largely immobile. Despite this difference, the plant actin cytoskeleton has a conserved function in vesicle trafficking and organelle movements (3). Compared to animals, the role of actin in cell size control is not clear and remains to be addressed. The phytohormone auxin is a crucial regulator of cell size control in plants (4). Several studies suggest that the plant-specific growth regulator auxin affects the actin cytoskeleton (5-10). These studies concentrated on the auxin effect on cortical actin and its contribution to processes close to the plasma membrane, such as endocytosis and exocytosis (5-11). Here we reveal that the actin cytoskeleton is also required for auxin processes beyond the plasma membrane, contributing to vacuolar morphogenesis and consequently to cell size regulation in plants.

Results and discussion

To assess the organization of actin filaments in root epidermal cells we used the actin marker Lifeact-Venus (a 17-amino-acid peptide fused to Venus, which stains filamentous (F-) actin structures (12)) and measured the density of actin in cortical sections of late meristematic cells. The exogenous application of auxin (NAA; 500 nM for 6 hr) led to a higher fluorescent intensity of Lifeact-Venus (Fig. S1 A-***F***) and, moreover, significantly increased the integrated density of actin filaments (Fig. 1 ***A-C***). This increase was sensitive to auxinole (13) a designated inhibitor of TIR1/AFBs auxin receptors (Fig. S1 ***G-L***). To further define the actin filament organisation beyond the cell cortex, we used gated stimulated emission depletion (gSTED) super resolution live cell imaging and performed defined z-stack imaging on epidermal root cells. Application of auxin (250 nM for 20 hr) increased the skewness of actin filaments in maximum projections (Fig. 1 ***D-F***), suggesting a higher degree of actin filament bundling (14) in entire cells. Our data suggests that auxin signalling influences actin-dependent processes also beyond the plasma membrane, leading to a more close-drawn network of actin filaments.

We have recently reported that auxin controls the morphogenesis of the largest plant organelle, the vacuole, in a TIR1/AFBs-dependent manner, which is required for auxin-induced growth repression (15). Using confocal microscopy, we detected the actin cytoskeleton in the vicinity of the vacuole (Fig. S2), which is consistent with the proteomic detection of actin with vacuoles (16, 17). Interference with actin affects transvacuolar strands formation (18, 19), raising the question of whether the actin network is mechanistically linked to vacuolar morphogenesis required for auxin-reliant growth repression. To assess the role of actin for vacuolar morphology in epidermal root cells, we first interfered with actin dynamics pharmacologically. Depolymerization of actin by Latrunculin B (LatB), induced roundish vacuolar structures (Fig. S3 ***A***, ***B***, ***E*** and ***F***). LatB treatments also reduced the size of the largest luminal structure which defines (width multiplied by length) the vacuolar morphology index (15) (Fig. S3***D***). Similarly, Jasplakinolide (JASP)-dependent stabilization of actin affected the vacuolar shape and increased the vacuolar morphology index (Fig. S3 ***A***, ***C***, ***E***, ***G*** and ***D***). Notably, the JASP effect on vacuoles was most pronounced in cells shortly before elongation. In contrast to interference with actin, microtubules were not enriched in the vicinity of the tonoplast (Fig. S2B, C) and oryzalin-induced depolymerisation of microtubule had no immediate effect on vacuolar morphology (Fig. S4). Our findings suggest that interference with actin but not microtubule dynamics affects the vacuolar morphology.

Based on this data, we assumed that the auxin effect on actin may also impact on vacuolar shape and, subsequently, addressed whether the actin cytoskeleton is required for the auxin-induced changes of vacuolar morphology. To approach this, we induced high and low auxin conditions in the presence of actin affecting drugs. Exogenous application of auxin leads to a significantly lower vacuolar morphology index in meristematic cells of the root epidermis (15) (Fig. 1 ***G***, ***H*** and ***J***). Complementary, we depleted cellular auxin by the application of the auxin biosynthesis inhibitor kynurenin (Kyn), which leads to a significantly higher vacuolar morphology index in wild type (15) (Fig. 1 ***G***, ***I*** and ***J***). In contrast, actin depolymerization and stabilization resulted in vacuoles that were less affected by auxin (Fig. 1 ***K***, ***L***, ***N*** and ***O***, ***P***, ***R***) and Kyn application (Fig. 1 ***K***, ***M***, ***N*** and ***O***, ***Q***, ***R***).

We accordingly conclude that pharmacological interference with actin abolishes auxin-induced changes of vacuolar morphology (Fig. 1 ***G-R***), suggesting that the actin cytoskeleton is mandatory in instructing both smaller and larger luminal

vacuoles. Corresponding with this pharmacological approach, moderate genetic interference with actin and its motor protein myosin distinctly reduced the auxin effect on vacuolar morphology. Actin mutants, such as ***act7-4*** (20) and ***act2/act8*** (21), as well as myosin mutants ***xi-k/1/2*** and ***xi-k/1/2/i*** (22), showed subcellular resistance to auxin, displaying partially insensitive vacuoles (Fig. 2 ***A***-***G*** and ***H***-***N***). This confirms that the actin-myosin system is required for the auxin effect on vacuolar morphology.

As previously reported, vacuolar morphology control is required for auxin-dependent growth repression (15). We therefore tested whether the subcellular resistance to auxin would also lead to auxin-resistant cellular elongation in actin and myosin mutants. We consequently recorded the maximum root epidermal cell expansion in the elongation zone of untreated and auxin treated seedlings. Auxin treatments (125nM for 20 hr) inhibited root epidermal expansion in wild type (Fig. 2 ***O***, ***P*** and ***U***), but genetic interference with actin and myosin induced a partial resistance to auxin (Fig. 2 ***Q***-***U***). Notably, mild pharmacological interference with actin, by low doses of LatB (125 nM for 20 hr), not affecting cellular elongation rates on its own, similarly blocked auxin-induced growth repression (Fig.2***V***; Fig.S3 ***H***-***K***). This data suggests that the actin cytoskeleton influences auxin-dependent vacuolar morphology required for cellular growth control.

Auxin controls the abundance of vacuolar SNARE complex components, which is required for its effect on vacuolar morphology and cellular growth repression (15). The root growth of the vacuolar SNARE mutant ***vti11*** was less affected than the wild type when germinated on LatB (100 nM) containing medium (Fig. S5 ***A*** and ***B***). This resistance could be due to altered vacuolar morphogenesis, because the ***vti11*** vacuoles remained larger when treated with LatB (Fig. S5 ***C-I***, compare ***C*** to ***G***). Notably, pharmacological inhibition of PI3- and PI4-kinases by wortmannin (WM; 33 µM; 6 hr) does not only interfere with auxin-induced stability of SNAREs (15), but also abolished the auxin (500 nM; 6 hr) effect on Lifeact-Venus density and abundance (Fig. S6 ***A-J***). On the other hand, genetic and pharmacological interference with phosphatidylinositols strongly reduced the effect of LatB (500 nM, 6hr) and JASP (2.5 µM; 6 hr) on vacuolar morphology (Fig. S6 ***K-T***). Nevertheless, LatB and JASP treatments did not block auxin-induced stabilisation of vacuolar SNARE VAMP711-GFP (Fig. S7). Even though this interaction demands further in depth

investigation, this set of data suggests that actin- and SNARE-dependent processes impact at least partially interdependent on auxin-controlled vacuolar morphology.

We subsequently addressed by which cellular mechanism the actin cytoskeleton affects vacuolar function. Auxin treatment seemingly leads to multiple small luminal vacuoles (15) and several studies have previously addressed the mechanisms of vacuolar fragmentation (16, 18, 23-25). Accordingly, actin and its motor protein myosin could contribute forces required for auxin-dependent vacuolar fission and fusion events. Conversely, other studies have revealed that several plant cells show interconnected vacuolar structures (26-31). Accordingly, the actin-myosin system could generate or release vacuolar constrictions. We therefore addressed whether auxin impacts either on the fragmentation or the constriction of the vacuole.

We hence employed serial block-face scanning electron microscopy (SBF-SEM) and 3D reconstruction to obtain a nanometre resolution of the epidermal cell vacuole. Untreated cells showed largely interconnected vacuolar cisternae (Fig. 3***A***, Movie S1). Similarly, auxin treated samples showed interconnected structures, but the vacuolar cisternae appeared much smaller and more numerous (Fig. 3***B***, Movie S2). This finding suggests that auxin does not primarily lead to vacuolar fragmentations, but to more constrictions. To quantitatively elaborate on this finding in living cells, we utilized Fluorescent Recovery After Photo-bleaching (FRAP) (27) on the luminal vacuole dye BCECF (32). Following its photo-bleaching, the luminal dye readily recovered in untreated epidermal cells (Fig. 3 ***C***-***E***, ***I***), confirming its mainly interconnected nature. Most vacuoles also showed FRAP in response to auxin, but the recovery was slower compared to untreated controls (Fig. 3 ***F***-***I***). The slower recovery substantiates auxin-induced constrictions of interconnected vacuoles, leading to a reduced rate of luminal diffusion through tubular structures. Notably, an increased fraction of vacuoles did not show recovery in the analysed time frame (Fig. S8 ***A*** and ***B***), suggesting that auxin also increases the occurrence of solitary vacuoles. Nevertheless, this set of data strongly indicates that auxin does not primarily lead to vacuolar fragmentation as initially implied from 2D imaging (15) (Fig. 1***H***), but rather to vacuolar constrictions.

To further unravel the importance of vacuolar constrictions, we used BCECF imaging to obtain a cellular view of the vacuolar volume. The vacuoles' size increases during cellular expansion, which was visibly suppressed by the application of auxin (Fig. S9 ***A*** and ***B***). Notably, auxin treatment strongly decreased the vacuolar volume

and consequently shifted the vacuole surface to volume ratio in late meristematic epidermal cells in wild type (Fig. 4 ***A***-***D***, Movies S3 and S4), but not following pharmacologic or genetic interference with actin/myosin (Fig. 4 ***E-M***). The ensuing assumption - that auxin might define how much cell space a vacuole occupies - led us to use MorphoGraphX (33) to measure vacuolar volume in relation to the cell volume. Intriguingly, auxin treatments restricted the cellular occupancy of the vacuole (Fig. 4 ***N***, ***O*** and ***V***). In contrast, the auxin effect on vacuolar occupancy was abolished by pharmacological or genetic interference with actin/myosin dynamics (Fig. 4 ***P***-***V***). We accordingly conclude that auxin negatively regulates the vacuolar volume in an actin-dependent manner, directly influencing the relative cellular occupancy of the vacuole.

Our work reveals that the actin cytoskeleton has a role in cell size control in plants. Actin is utilized in a plant-specific growth mechanism by controlling the volume of the largest plant organelle, the vacuole. Low and high auxin levels can expand and constrict the plant vacuole, respectively. Vacuolar SNAREs are involved in this process (15) and appear to interact with actin-dependent processes. Notably, several SNARE proteins seem to physically interact with actin (34), but whether such an interaction impacts on vacuolar morphogenesis remains to be investigated. We illustrate that auxin induces a more close drawn arrangements of actin filaments, which may physically restrict the expansion of vacuoles. However, we cannot rule out that actin-dependent vesicle transport also contributes to vacuolar shapes. Actin and myosin mutants are partially resistant to auxin, presumably due to their inability to implement auxin-induced changes in actin cytoskeleton. Rather unexpectedly, we report that in late meristematic cells of the root epidermis the vacuolar shape mainly depends on actin-dependent constrictions and not homotypic fusions. Moreover, we have revealed that actin ***is*** actually required for the auxin-dependent cellular occupancy of the vacuole. It is conceivable that the vacuole has an important space-filling function during growth and we hypothesize that this mechanism allows a plant cell to elongate without altering its cytosolic matter. This tallies with previous findings that the cytosolic content does not correlate with cell size in plant cell cultures (35). Accordingly, auxin would limit intracellular expansion of the vacuole to restrict cellular growth potential.

In protists, the contractile vacuole regulates the quantity of water in a cell (36). It is possible that vacuoles maintain a related role in multicellular organisms, such as fungi, algae and land plants. What these organisms have in common is that they show

rapid cellular elongation rates by massive cellular uptake of water, which possibly risks cytosol dilution. Although water and soluble fluxes between the cytosol and vacuolar lumen remain to be addressed in our experimental set up, it is tempting to postulate that vacuole enlargement could compensate for this cellular flooding, in a partially actin-dependent manner. Accordingly, we propose a cellular growth model in which auxin restricts the vacuolar volume presumably required for cytosol homeostasis during cellular expansion.

Methods

Plant Materials and Growth Conditions. ***Arabidopsis thaliana***, ecotype ***Columbia 0*** (***Col-0***) was used. The following plant lines were published previously: 35S::Lifeact-Venus (37), 35S::GFP-ABD2 (38, 39), 35S::MAP4-GFP (40), ***act7-4*** (20), ***pUBQ10::YFP-VAMP711*** (Wave 9Y/R) (41), ***act2-1/act8-2*** (21)***, xi-k/1/2*** and ***xi-k/1/2/I*** (22), ***pi4kß1/2*** (42) and ***vti11*** (43). Seeds were stratified at 4°C for 2 days in the dark and grown on vertically orientated ½ Murashige and Skoog (MS) medium plates under a long-day regime (16 hr light/8 hr dark) at 20–22°C.

Chemicals. All chemicals were dissolved in DMSO and were applied in solid or liquid ½ MS-medium. Dyes were applied in liquid ½ MS-medium before imaging. 1-naphthaleneacetic acid (NAA or 1-NAA)and 2-naphthaleneacetic acid (2-NAA) was obtained from Duchefa (Netherlands), FM4-64, L-kynurenine (Kyn), Latrunculin B (LatB) and propidium iodide (PI) from Sigma-Aldrich (MO, USA), BCECF-AM, MDY-64 and Jasplakinolide (JASP) from Life Technologies (CA, USA). Wortmannin (WM) was obtained from Cayman Chemical (MI, USA) and auxinole was kindly provided by Ken-ichiro Hayashi (13).

Phenotype Analysis. For the quantification of vacuolar morphology and cell length change, 7-day-old seedlings were used. To analyze the vacuolar morphology index, subcortical confocal sections (above the nucleus) of the root epidermis were acquired (according to Löfke et al., 2015) and further processed with ImageJ software (http://rsb.info.nih.gov/ij/). Images were taken in the late meristematic zone, as published before (15). For JASP treatments mainly cells shortly before onset of elongation (below transition zone) were quantified. The largest luminal structures in five epidermal atrichoblast cells were quantified by measuring the longest and widest

distance and processed by multiplying the values (termed Vacuolar Morphology Index - 15). Quantification of final cell length change in elongated epidermal root hair cells was carried out on median confocal sections. To estimate positions for cell length measurements in the elongation zone, seedlings were stained in PI (0.02 mg/ml) for 5 min, and subsequently images were acquired where no PI entered the vasculature, depicting differentiated endosomal diffusion barriers (15). The quantification of integrated density was carried out using cortical sections of root epidermal cells. Integrated density was determined using the respective analysis option in ImageJ. For signal intensity measurements (mean grey value) of the actin cytoskeleton a rectangle of 4000 μm^2 was drawn in the meristematic zone of the root and the mean grey value of 15-20 cells per conditions was analyzed. For every treatment a minimum of 75 cells were considered. For analysis of the root length, seedlings grown on vertically orientated plates were scanned on a flat-bed scanner and measurements were performed in ImageJ. Per condition 15-20 seedlings were analyzed 8 days after germination for each experiment.

Confocal Microscopy. For live cell imaging, six-day-old seedlings were used. For image acquisition a Leica SP5 (DM6000 CS), TCS AOBS confocal laser scanning microscope was used, equipped with a Leica HC PL APO CS 20×0.70 IMM UV objective or a Leica HCX PL APO CS 63×1.20 water immersion objective. MDY-64 was excited at 458 nm (fluorescence emission: 465 – 550 nm), GFP and BCECF at 488 nm (fluorescence emission: 500 – 550 nm), YFP at 514 nm (fluorescence emission: 525 – 578 nm) and FM4-64 and PI at 561 nm (fluorescence emission for FM4-64: 599 – 680; for PI: 644 – 753 nm). Whenever vacuolar morphology was analyzed, roots were mounted in propidium iodide (PI) solution (0.02 mg/ml) to counterstain cell walls. MDY-64, FM4-64 and BCECF staining was performed as described previously (32). Z-stacks were recorded with a step size of 420 nm, resulting in 25-35 Z-stack images per cell. Three-dimensional surface renderings, using vacuoles loaded with BCECF-AM were achieved using the ImageJ plug-in 3-D Viewer (http://rsb.info.nih.gov/ij/). We used MorphoGraphX (33) to segment 3D cell boundaries (based on PI signal), which allowed us to depict the cell volume in relation to vacuolar volume (based on the BCECF signal). Imaging and rendering settings were constant within an experiment.

FRAP Measurements. For FRAP measurements, a Leica TCS SP5II microscope equipped with a HCX PL APO lambda blue 63.0x1.20 WATER UV water immersion objective was used. ***Arabidopsis*** seedlings (5 DAG) were incubated for 18h in liquid ½ MS medium supplemented with 250 nM NAA or the corresponding volume of DMSO. 15 hours into incubation, membrane-permeant BCECF-AM (10 µM; Molecular Probes, Invitrogen) was added for 2 hours. The seedlings were then washed for 1 hour in their respective solution without BCECF, and imaged afterwards. FRAP experiments were carried out with the FRAP Wizard implemented in the Leica LAS AF software. The area of interest was selected and bleached using the "Bleach Point" mode. All experiments consisted of 4 pre-bleach frames, a point bleach step for 250 ms with a laser power between 30 % and 50 % and subsequent 40 to 50 frames of post-bleach acquisition. Image acquisition was performed at a scanning speed of 1400Hz (bidirectional scanning), a resolution of 512x512 pixels at a zoom-factor of 6 (pixel size 80.2 nm x 80.2 nm) and a line-average of 3. BCECF was excited at 488 nm and its emission detected with a Hybrid detector (standard mode) between 495 nm and 560 nm. The point bleach area was used to measure FRAP. Calculations of the recovery halftime were done with the FRAP Profiler plug-in for ImageJ. The boxplots were generated with OriginPro 2015 (OriginLab).

Super-resolution Microscopy. For image acquisition, an inverted Leica SP8 (DMi8) microscope, equipped with a gated STED module (gSTED), operating with a depletion laser at 592 nm wavelength was used. For excitation of Lifeact-Venus, a pulsed supercontinuum laser (white light laser, WLL II) was used at 510 nm. Emission fluorescence was detected with a HyD detector at 525 nm – 578 nm). The Leica HC PL APO CS2 100×1.4 objective was used. Pixel dwell time was between 500 nm and 1 µm. To quantify auxin-mediated changes of the cytoskeleton organization, we measured the skewness of Lifeact-Venus-marked actin filaments. For that, z-stacks (step size 0.42 µm, 25-35 sections/stack) of entire meristematic cells were acquired and subsequently processed with ImageJ (http://rsb.info.nih.gov/ij/). All z-stack images were skeletonized, projected and the skewness of the actin filaments measured as described previously (14), indicating the degree of actin bundling.

Scanning Electron Microscopy. Arabidopsis seedlings roots were cut off and submerged in fixative (1% PFA, 1% GA, 2% sucrose and 2mM CaCl in 0.1 M NaCac buffer) for 1 hr at room temperature, processed using the zinc iodide osmium impregnation technique and embedded in Spurr resin (44). Root tips were then mounted onto 3view stubs (Gatan) with Conductive Epoxy (Chemtronics) and hardened for 4 hours at 100 °C. The final trimmed block was sputter coated with gold for 30 sec (layer thickness ~ 20 nm) to improve conductivity. Serial block face SEM images were collected on a Merlin Compact SEM (Zeiss) with the Gatan 3view system. Section thickness was set to 100 nm and the block face was imaged in variable pressure mode (~50 Pa) at 4kV acceleration voltage with a pixel dwell time of 7-8 µs and pixel size of 0.009 µm (***Col-0***) and 0.015 µm (***Col-0***+NAA).Data processing (stack formation, image alignment, trimming and scaling sections to common mean and standard deviation) was done in the imod software package (45). Amira software (FEI) magic wand tool was used to select the vacuoles throughout the entire cell. Areas with ZIO deposits in the vacuoles that blocked selection by the magic wand tool were manually added to the material by using the brush tool. The contours were twice smoothened with a filter mask size 5. The 3D model was visualized using surface generation and surface view.

Analysis and Data Presentation. All experiments were carried out at least three times. Replicates were biological replicates from different plants. All figures display representative experiments and sample size is given in the figure legend for each experiment. Data are shown as mean ± SEM. Statistical significance was evaluated by the Student's ***t***-test using graphpad (http://www.graphpad.com/quickcalcs/).

ACKNOWLEDGEMENTS

We thank Valerian Dolja, Elison B. Blancaflor, Richard J. Cyr, Nico Geldner, Takashi Ueda, Ken-ichiro Hayashi, Erik Nielson, Masao Tasaka, and Richard B. Meagher for providing published material. We are grateful to the BOKU-VIBT Imaging Centre for access and expertise. We would like to thank David Whittaker for help with the manuscript and Elsa Arcalis for technical support and advice. This work was supported by the Vienna Science and Technology Fund (WWTF) (Vienna Research Group), Austrian Science Fund (FWF) (P26568-B16 and P26591-B16) and the European Research Council (ERC) (Starting Grant 639478-

AuxinER) (to J.K-V.), as well as the Deutsche Forschungsgemeinschaft (DFG) (personal postdoctoral fellowships to D.S. and C.L.). The BBSRC are acknowledged for ALERT13 funding of the SBFSEM (BB/C014122/1) (to C.H.).

AUTHOR CONTRIBUTIONS

D.S., C.H., K.S., and J.K-V designed research. D.S., C.L., F.K., M.K., A.E., and L.H. performed research. D.S., C.L., F.K., M.K., R.S. and J.K- V. analyzed data. D.S. and J.K- V. wrote the paper and all authors saw and commented on the manuscript.

REFERENCES

1. Fletcher DA & Mullins RD (2010) Cell mechanics and the cytoskeleton. *Nature* 463(7280):485-492.
2. Faix J, *et al.* (1996) Cortexillins, major determinants of cell shape and size, are actin-bundling proteins with a parallel coiled-coil tail. *Cell* 86(4):631-642.
3. Thomas C & Staiger CJ (2014) A dynamic interplay between membranes and the cytoskeleton critical for cell development and signaling. *Frontiers in plant science* 5:335.
4. Sauer M, Robert S, & Kleine-Vehn J (2013) Auxin: simply complicated. *Journal of experimental botany* 64(9):2565-2577.
5. Rahman A, *et al.* (2007) Auxin, actin and growth of the Arabidopsis thaliana primary root. *The Plant journal : for cell and molecular biology* 50(3):514-528.
6. Dhonukshe P, *et al.* (2008) Auxin transport inhibitors impair vesicle motility and actin cytoskeleton dynamics in diverse eukaryotes. *Proceedings of the National Academy of Sciences of the United States of America* 105(11):4489-4494.
7. Nick P, Han MJ, & An G (2009) Auxin stimulates its own transport by shaping actin filaments. *Plant physiology* 151(1):155-167.
8. Nagawa S, *et al.* (2012) ROP GTPase-dependent actin microfilaments promote PIN1 polarization by localized inhibition of clathrin-dependent endocytosis. *PLoS biology* 10(4):e1001299.
9. Lanza M, *et al.* (2012) Role of actin cytoskeleton in brassinosteroid signaling and in its integration with the auxin response in plants. *Developmental cell* 22(6):1275-1285.
10. Li G, *et al.* (2014) Rice actin-binding protein RMD is a key link in the auxin-actin regulatory loop that controls cell growth. *Proceedings of the National Academy of Sciences of the United States of America* 111(28):10377-10382.
11. Zhu J & Geisler M (2015) Keeping it all together: auxin-actin crosstalk in plant development. *Journal of experimental botany*.
12. Riedl J, *et al.* (2008) Lifeact: a versatile marker to visualize F-actin. *Nature methods* 5(7):605-607.

13. Hayashi K*, et al.* (2012) Rational design of an auxin antagonist of the SCF(TIR1) auxin receptor complex. *ACS chemical biology* 7(3):590-598.
14. Higaki T, Kutsuna N, Sano T, Kondo N, & Hasezawa S (2010) Quantification and cluster analysis of actin cytoskeletal structures in plant cells: role of actin bundling in stomatal movement during diurnal cycles in Arabidopsis guard cells. *The Plant journal : for cell and molecular biology* 61(1):156-165.
15. Löfke C, Dünser K, Scheuring D, & Kleine-Vehn J (2015) Auxin regulates SNARE-dependent vacuolar morphology restricting cell size. *eLife* 4.
16. Mathur J, Mathur N, Kernebeck B, & Hulskamp M (2003) Mutations in actin-related proteins 2 and 3 affect cell shape development in Arabidopsis. *The Plant cell* 15(7):1632-1645.
17. Carter C*, et al.* (2004) The vegetative vacuole proteome of Arabidopsis thaliana reveals predicted and unexpected proteins. *The Plant cell* 16(12):3285-3303.
18. Li J*, et al.* (2012) Capping protein modulates the dynamic behavior of actin filaments in response to phosphatidic acid in Arabidopsis. *The Plant cell* 24(9):3742-3754.
19. Staiger CJ*, et al.* (1994) Microinjected profilin affects cytoplasmic streaming in plant cells by rapidly depolymerizing actin microfilaments. *Current biology : CB* 4(3):215-219.
20. Gilliland LU, Pawloski LC, Kandasamy MK, & Meagher RB (2003) Arabidopsis actin gene ACT7 plays an essential role in germination and root growth. *The Plant journal : for cell and molecular biology* 33(2):319-328.
21. Kandasamy MK, McKinney EC, & Meagher RB (2009) A single vegetative actin isovariant overexpressed under the control of multiple regulatory sequences is sufficient for normal Arabidopsis development. *The Plant cell* 21(3):701-718.
22. Peremyslov VV, Prokhnevsky AI, & Dolja VV (2010) Class XI myosins are required for development, cell expansion, and F-Actin organization in Arabidopsis. *The Plant cell* 22(6):1883-1897.
23. Novakova P*, et al.* (2014) SAC phosphoinositide phosphatases at the tonoplast mediate vacuolar function in Arabidopsis. *Proceedings of the National Academy of Sciences of the United States of America* 111(7):2818-2823.
24. Cui Y*, et al.* (2014) Activation of the Rab7 GTPase by the MON1-CCZ1 Complex Is Essential for PVC-to-Vacuole Trafficking and Plant Growth in Arabidopsis. *The Plant cell* 26(5):2080-2097.
25. Zheng J, Han SW, Rodriguez-Welsh MF, & Rojas-Pierce M (2014) Homotypic vacuole fusion requires VTI11 and is regulated by phosphoinositides. *Molecular plant* 7(6):1026-1040.
26. Mitsuhashi N, Shimada T, Mano S, Nishimura M, & Hara-Nishimura I (2000) Characterization of organelles in the vacuolar-sorting pathway by visualization with GFP in tobacco BY-2 cells. *Plant & cell physiology* 41(9):993-1001.
27. Gao XQ*, et al.* (2005) The dynamic changes of tonoplasts in guard cells are important for stomatal movement in Vicia faba. *Plant physiology* 139(3):1207-1216.

28. Reisen D, Marty F, & Leborgne-Castel N (2005) New insights into the tonoplast architecture of plant vacuoles and vacuolar dynamics during osmotic stress. *BMC plant biology* 5:13.
29. Ruthardt N, Gulde N, Spiegel H, Fischer R, & Emans N (2005) Four-dimensional imaging of transvacuolar strand dynamics in tobacco BY-2 cells. *Protoplasma* 225(3-4):205-215.
30. Tanaka Y, *et al.* (2007) Intra-vacuolar reserves of membranes during stomatal closure: the possible role of guard cell vacuoles estimated by 3-D reconstruction. *Plant & cell physiology* 48(8):1159-1169.
31. Viotti C, *et al.* (2013) The endoplasmic reticulum is the main membrane source for biogenesis of the lytic vacuole in Arabidopsis. *The Plant cell* 25(9):3434-3449.
32. Scheuring D, Schöller M, Kleine-Vehn J, & Löfke C (2015) Vacuolar staining methods in plant cells. *Methods in molecular biology* 1242:83-92.
33. Barbier de Reuille P, *et al.* (2015) MorphoGraphX: A platform for quantifying morphogenesis in 4D. *eLife* 4:05864.
34. Fujiwara M, *et al.* (2014) Interactomics of Qa-SNARE in Arabidopsis thaliana. *Plant & cell physiology* 55(4):781-789.
35. Owens T & Poole RJ (1979) Regulation of cytoplasmic and vacuolar volumes by plant cells in suspension culture. *Plant physiology* 64(5):900-904.
36. Docampo R, Jimenez V, Lander N, Li ZH, & Niyogi S (2013) New insights into roles of acidocalcisomes and contractile vacuole complex in osmoregulation in protists. *International review of cell and molecular biology* 305:69-113.
37. Era A, *et al.* (2009) Application of Lifeact reveals F-actin dynamics in Arabidopsis thaliana and the liverwort, Marchantia polymorpha. *Plant & cell physiology* 50(6):1041-1048.
38. Sheahan MB, Rose RJ, & McCurdy DW (2004) Organelle inheritance in plant cell division: the actin cytoskeleton is required for unbiased inheritance of chloroplasts, mitochondria and endoplasmic reticulum in dividing protoplasts. *The Plant journal : for cell and molecular biology* 37(3):379-390.
39. Wang YS, Motes CM, Mohamalawari DR, & Blancaflor EB (2004) Green fluorescent protein fusions to Arabidopsis fimbrin 1 for spatio-temporal imaging of F-actin dynamics in roots. *Cell motility and the cytoskeleton* 59(2):79-93.
40. Marc J, *et al.* (1998) A GFP-MAP4 reporter gene for visualizing cortical microtubule rearrangements in living epidermal cells. *The Plant cell* 10(11):1927-1940.
41. Geldner N, *et al.* (2009) Rapid, combinatorial analysis of membrane compartments in intact plants with a multicolor marker set. *The Plant journal : for cell and molecular biology* 59(1):169-178.
42. Preuss ML, *et al.* (2006) A role for the RabA4b effector protein PI-4Kbeta1 in polarized expansion of root hair cells in Arabidopsis thaliana. *The Journal of cell biology* 172(7):991-998.
43. Yano D, *et al.* (2003) A SNARE complex containing SGR3/AtVAM3 and ZIG/VTI11 in gravity-sensing cells is important for Arabidopsis shoot

gravitropism. *Proceedings of the National Academy of Sciences of the United States of America* 100(14):8589-8594.
44. Hawes CR, Juniper BE, & Horne JC (1981) Low and high voltage electron microscopy of mitosis and cytokinesis in maize roots. *Planta* 152(5):397-407.
45. Kremer JR, Mastronarde DN, & McIntosh JR (1996) Computer visualization of three-dimensional image data using IMOD. *Journal of structural biology* 116(1):71-76.

Figure legends:

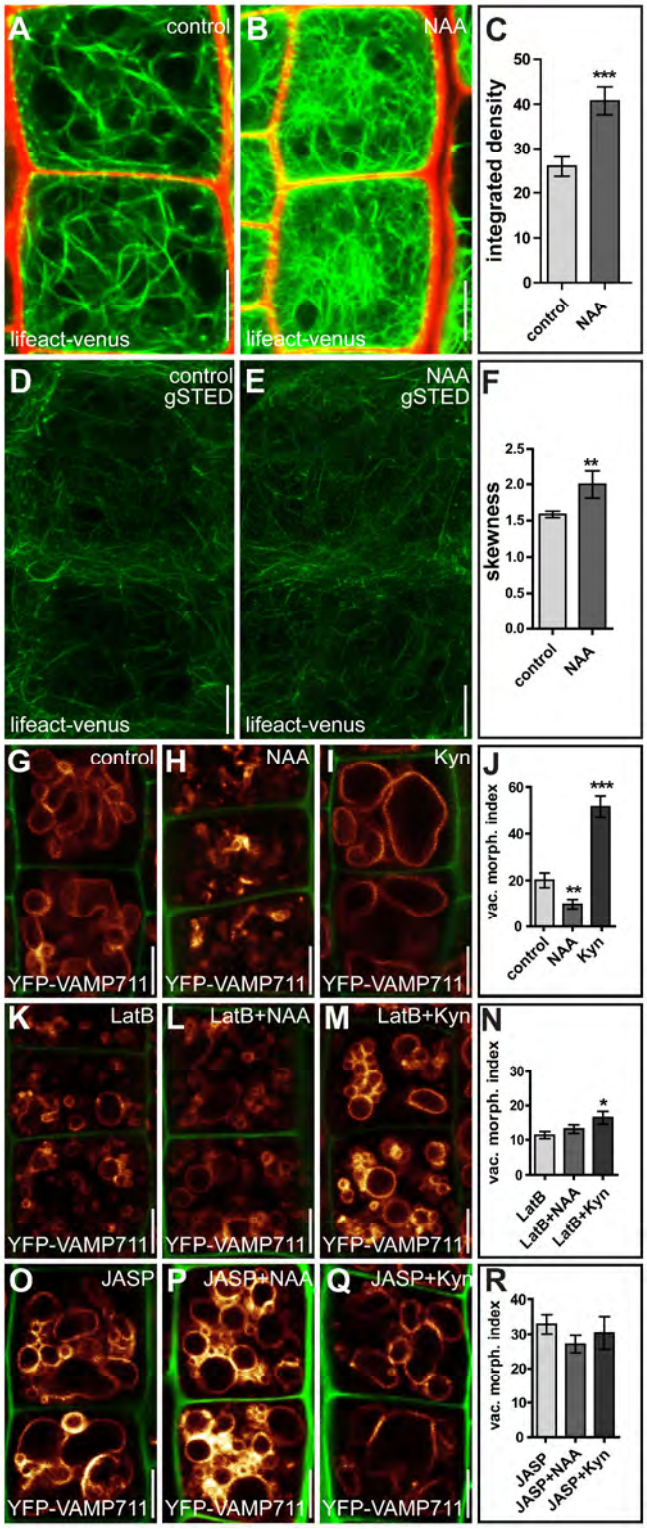

Fig. 1. Auxin impacts on the actin cytoskeleton and on actin-dependent vacuolar morphology. (***A-C***) Measurements of the integrated density of actin filaments (Lifeact-Venus) in cortical sections of root epidermal cells. DMSO (solvent control) (A) compared to auxin (NAA; 250 nM for 6 hr) treated (***B***) cells. (***C***) Quantification of the integrated density of actin filaments. (***D*** and ***E***) gated-STED super-resolution

microscopy of actin filaments of DMSO (***D***) and auxin (NAA; 250 nM for 20 hr) treated (***E***) root epidermal cells. (***F***) Skewness quantification of actin filament organization. (***G-I***) Control seedlings (DMSO) (***G***) compared to auxin (NAA; 500 nM; 6 hr) (***H***) and kynurenine (Kyn; 2 µM; 6 hr) treated (***I***) seedlings. (***J***) Vacuolar morphology (vac. morph. [µm2]) index depicts auxin effects on vacuolar appearance. (***K-M***) Latrunculin B (LatB; 500 nM; 6 hr) treatment led to more roundish vacuolar structures (***K***) and imposed reduced response to auxin (***L***) and kynurenin (***M***) treatment. Quantification of the vacuolar morphology index (***N***). (***O-Q***) Jasplakinolide (JASP; 2.5 µM; 6 hr) treatment led to distorted vacuolar structures (***O***), which imposed partial resistance to auxin (***P***) and kynurenin (***Q***) co-treatment. Quantification of the vacuolar morphology index (***R***). Data represent means ± SEM (***n*** = 35-70 cells for C, 10 z-stacks for ***F*** and ***n*** = 30 cells from six individual seedlings for ***J, N,*** and ***R***). YFP-VAMP711 (orange) and propidium iodide (PI; green) were used to highlight the vacuole and the cell wall, respectively. *$p < 0.05$, **$p < 0.01$, ***$p < 0.001$. Scale bar: 5 µm.

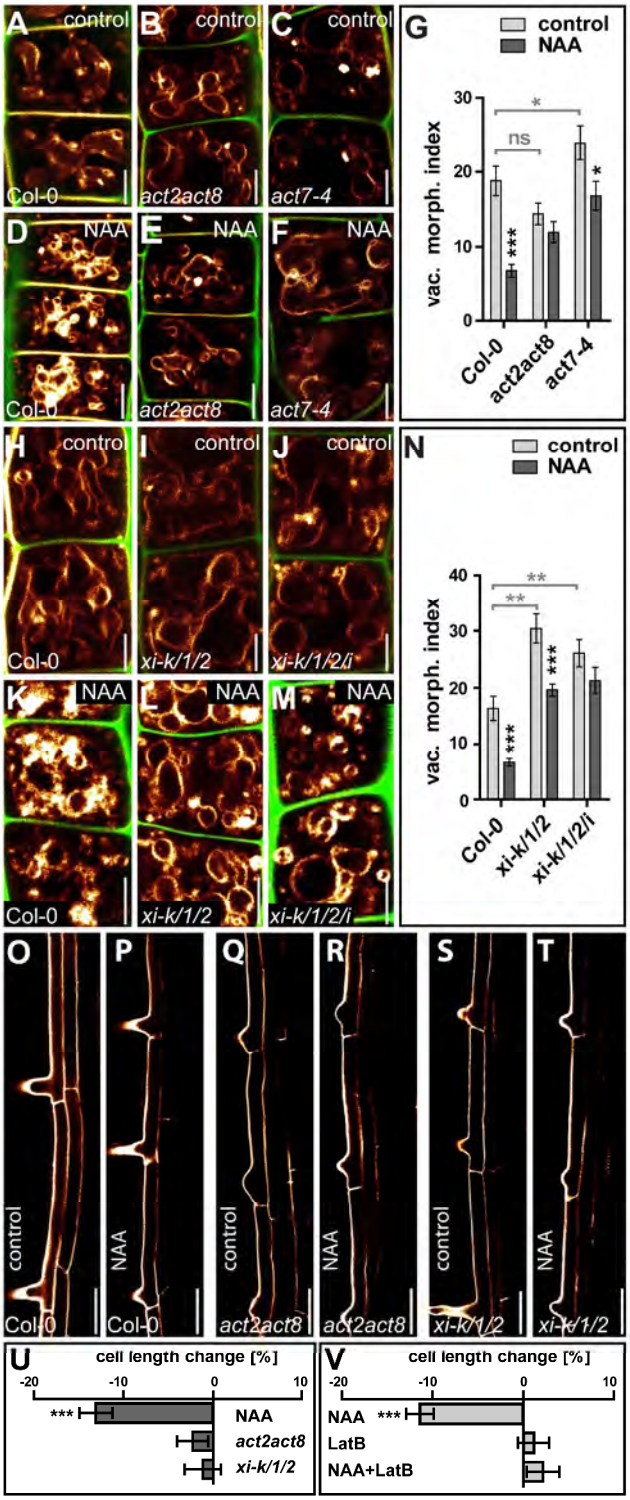

Fig. 2. Genetic interference with the actin-myosin system abolishes the auxin effect on vacuolar morphology and cellular growth rates. (***A-C***) DMSO solvent controls of ***Col-0*** wild type (***A***), the actin double-mutant ***act2act8*** (***B***) and the ***act7-4*** single mutant (***C***). (***D-F***) Auxin (NAA; 250 nM for 20 hr) treatment of ***Col-0*** (D), ***act2act8*** (***E***) and ***act7-4*** (***F***) seedlings. The vacuolar morphology (vac. morph. [µm2]) index strongly decreased in control plants, whereas actin mutants were less affected by

auxin (***G***). (***H-J***) DMSO solvent controls of ***Col-0*** (***H***), the myosin triple (***xi-k/1/2***) (***I***) and quadruple (***xi-k/1/2/i***) (***J***) mutants. (***K-M***) Auxin treatment of ***Col-0*** (K), ***xi-k/1/2*** (***L***) and ***xi-k/1/2/i*** (***M***) seedlings. While the vacuolar morphology index significantly decreased in control plants, myosin mutants were only mildly affected by auxin (***N***). (***O-V***) Cell length changes in fully elongated root cells in the differentiation zone. Untreated (DMSO) (***O***) and auxin (***P***) treated ***Col-0*** wild type seedlings show reduction in cell length (***U***). Neither the actin ***act2act8*** (***Q*** and ***R***) nor ***xi-k/1/2*** (***S*** and ***T***) showed a significant reduction in cell length change upon auxin treatment (***U***). Pharmacological interference with actin by Latrunculin B (LatB; 125 nM; 20hr) similarly blocked auxin-induced growth repression (***V***). Data represent means ± SEM (***n*** = 30 cells from six individual seedlings for ***G, N*** and ***n = 35*** cells from 9 individual roots for ***U***, ***V)***. The MDY-64 stain (orange) and the propidium iodide stain (PI; green) were used to highlight the vacuole and the cell wall, respectively. Light grey bars and asterisks in ***G*** and ***N*** indicate statistical evaluation based on untreated vacuoles. ns = not significant; *$p < 0.05$, ***$p < 0.001$. Scale bar: ***A-M*** = 5 µm; ***O-T*** = 50 µm.

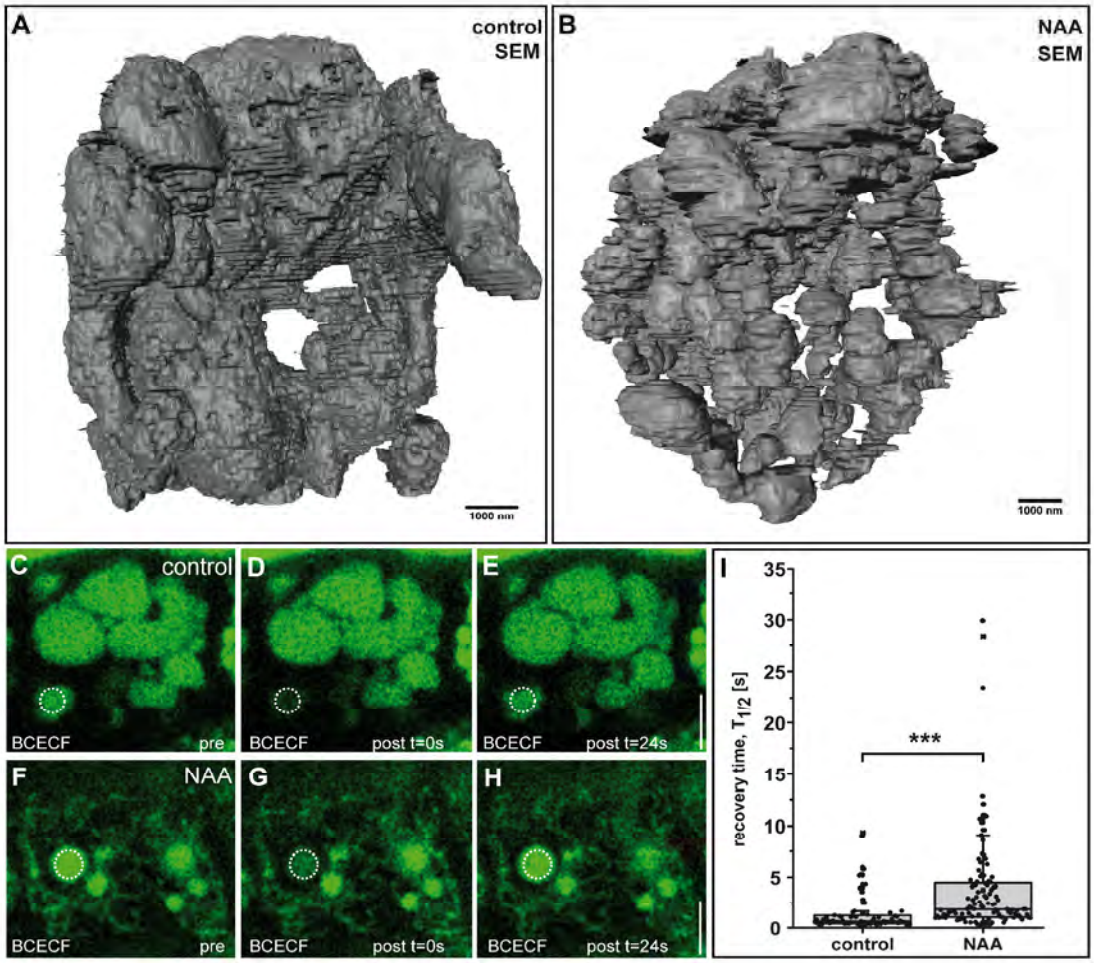

Fig. 3. Auxin induces vacuolar constrictions**.** (***A*** and ***B***) Scanning electron microscopy (SEM) based rendered vacuoles of DMSO solvent (***A***) and auxin (NAA; 250 nM for 20 hr) (***B***) treated ***Arabidopsis*** root epidermal cells. (***C-H***) Fluorescent Recovery After Photobleaching (FRAP) measurements of DMSO solvent control (***C-E***) and auxin (NAA; 250 nM for 18 hr) treated (***F-H***) ***Col-0*** seedlings stained with BCECF-AM. The FRAP recovery time after auxin treatment was significantly longer than in untreated seedlings (***I***). Data are represented as boxplot ± SD (***n*** = 70 bleached structures for the control and ***n*** = 112 bleached structures for auxin treatment. ***p < 0.001. Scale bars: ***A*** and ***B*** = 1000 nm; ***C-H*** = 5 µm.

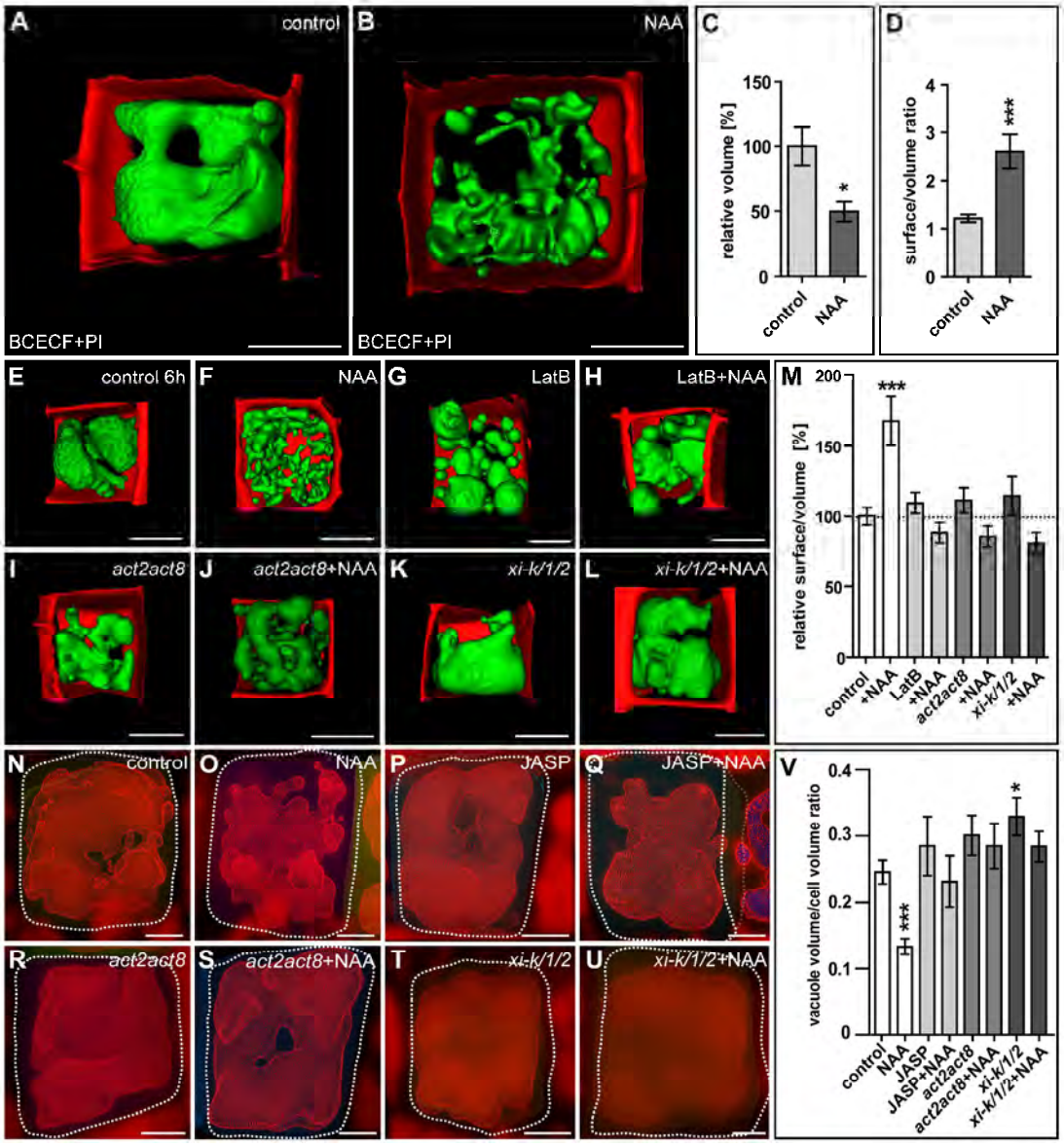

Fig. 4. Auxin controls the actin-dependent cellular occupancy of the vacuole. (***A*** and ***B***) Surface renderings of vacuoles of control (DMSO) (***A***) and auxin (NAA; 250 nM for 20 hr) treated (***B***) ***Col-0*** seedlings, stained with BCECF-AM (green), and propidium iodide (PI; red). (***C***) Quantification of relative vacuole volume and surface to volume ratio (***D***) for control and auxin treatment. (***E-H***) Surface renderings of vacuoles after control (DMSO) (***E***), auxin (NAA; 500 nM for 6 hr) (***F***), and Latrunculin B (LatB; 500 nM; 6 hr) (***G***) treatments, as well as LatB and auxin co-treatments (***H***). (***I-L***) Surface renderings of DMSO treated ***act2act8*** (***I***) and ***xi-k/1/2*** (***K***) as well as auxin treated ***act2act8*** (***J***) and ***xi-k/1/2*** (***L***) mutants. (***M***) Surface to volume ratio. (***N-U***) MorphoGraphX-based cellular and vacuolar segmentation to quantify its volume in control (DMSO) (***N***), auxin (***O***), Jasplakinolide (JASP; 2.5 µM; 6 hr) (***P***) and JASP and NAA co-treated (***Q***) cells. (***R-U***) Cellular and vacuolar

segmentation of DMSO treated ***act2act8*** (***R***) and ***xi-k/1/2*** (***T***) in comparison to auxin treatment (***S*** and ***U***). MorphoGraphX software was used to measure vacuolar volume in respect to cellular volume (***V***). Data represent means ± SEM (***n*** = 10 z-stacks from five individual seedlings for every condition for ***C, D, M*** and n > 11 cells for ***V***). *p < 0.05, ***p < 0.001. Scale bar= 5 µm.

Supplementary figure legends:

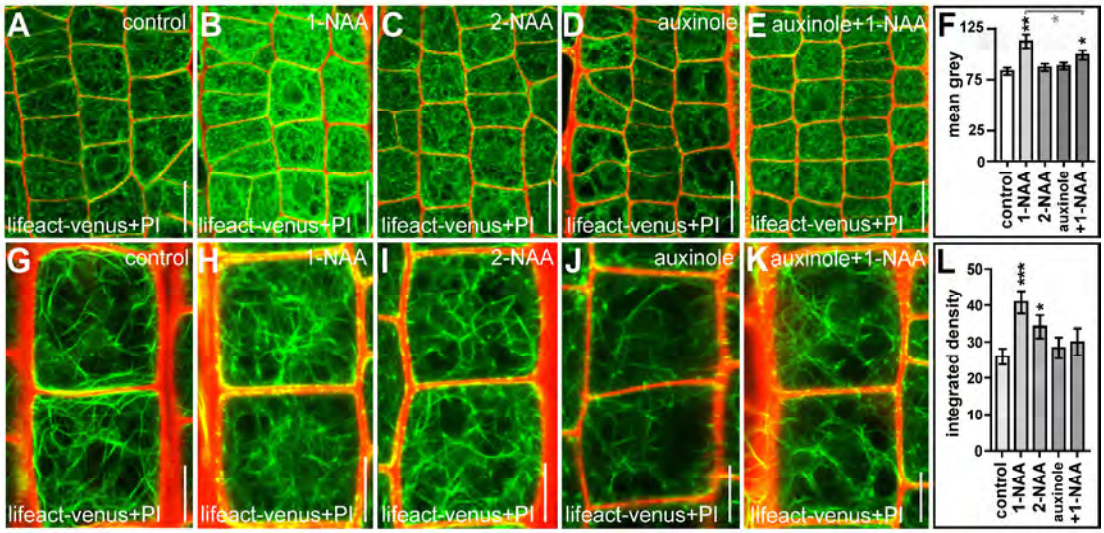

Fig. S1. Auxin-induced changes of the actin cytoskeleton are sensitive to auxinole. (***A-E***) Control seedlings (DMSO) (***A***) compared to 1-naphthaleneacetic acid (1-NAA; 500 nM; 6 hr) treated (***B***), 2-naphthaleneacetic acid (2-NAA; 500 nM; 6 hr) treated (***C***), auxinole (20 µM; 6 hr) treated (***D***) as well as auxinole and 1-NAA co-treated (***E***) seedlings. Please note that the auxin analogue 2-NAA has a lower affinity to TIR1/AFBs and that auxinole is engineered to specifically block TIR1/AFBs. Quantification of signal intensity of the actin marker Lifeact-Venus (***F***). (***G-K***) Respective treatments were used to determine the integrated density of actin filaments. DMSO control (***G***), 1-NAA (***H***), 2-NAA (***I***), and auxinole (***J***) treated as well as auxinole and 1-NAA co-treated (***K***) seedlings are shown. Quantification of the respective treatments (***L***). Data represent means ± SEM (***n*** = 75 meristematic cells from five individual seedlings for ***F and n*** = 35-70 cells from 6-10 individual seedlings for ***L***). Lifeact-Venus (green) and propidium iodide (PI; red) were used to highlight actin filaments and the cell wall, respectively. The light grey bar and asterisk in ***F*** indicates statistical evaluation of 1-NAA treatment compared to auxinole and 1-NAA co-treatment. *p < 0.05, ***p < 0.001. Scale bar: ***A-E*** = 15 µm; ***G-K*** = 15 µm.

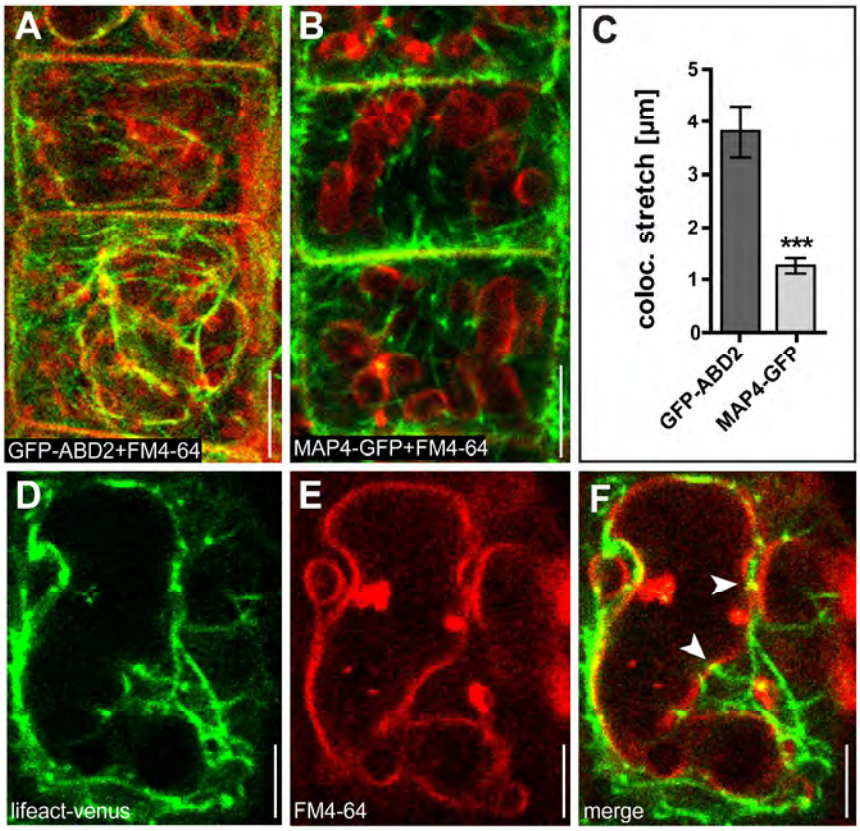

Fig. S2. The actin cytoskeleton and tonoplast are in close proximity. (***A*** and ***B***) Actin filaments, marked by GFP-ABD2 (***A***), are in close proximity to the FM4-64 (red) stained vacuolar membrane (tonoplast). Compared to the microtubule marker MAP4-GFP (***B***), stretches of colocalization of GFP-ABD2 with the tonoplast are significantly longer (***C***). Actin filaments, marked by Lifeact-Venus (***D***) and FM4-64 stained tonoplast (***E***). Arrowheads indicate potential contact sites of actin filaments at the tonoplast (***F***). Data represent means ± SEM (***n*** = 25 meristematic cells for ***C***). ***p < 0.001. Scale bar: 5 µm.

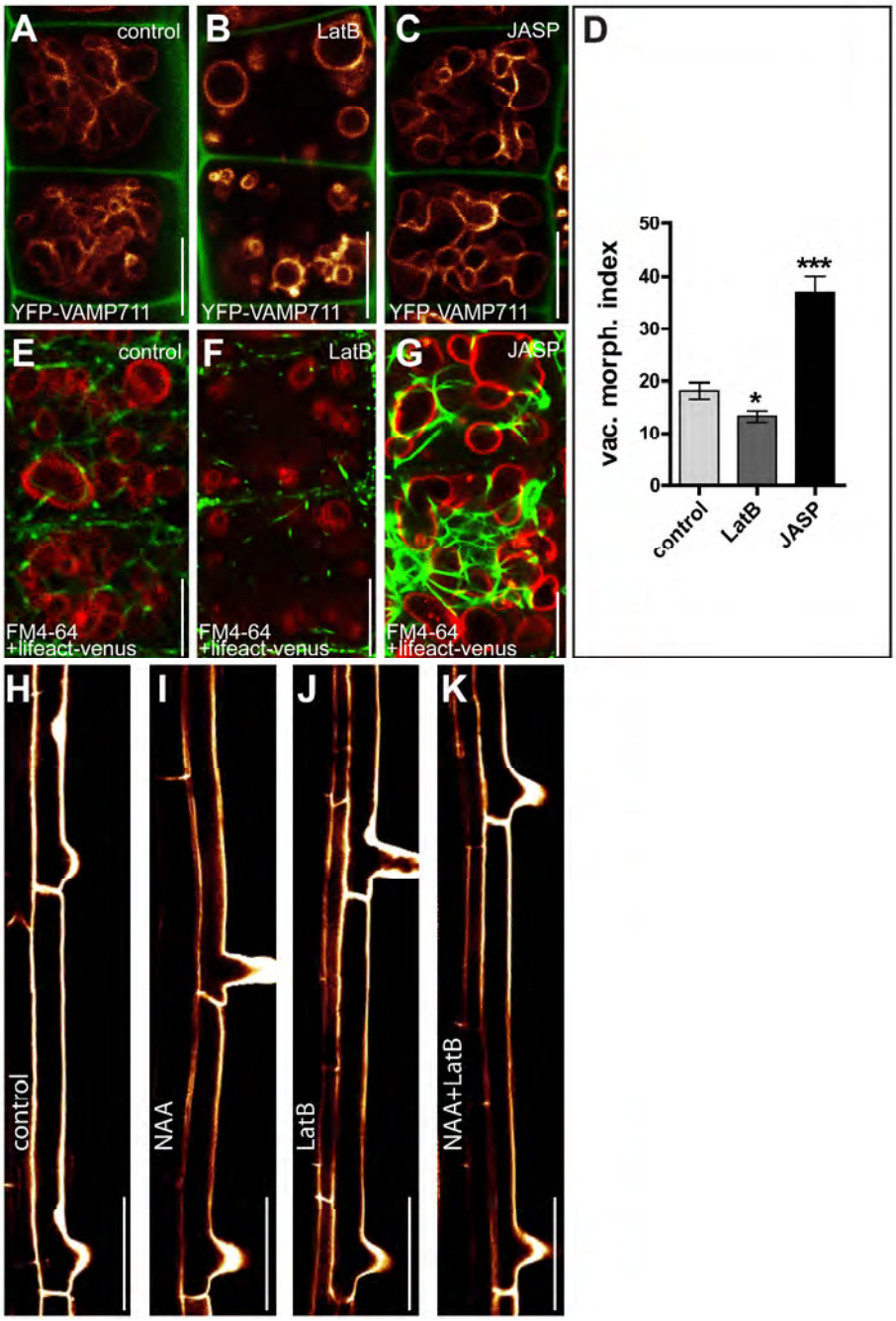

Fig. S3. Interference with the actin cytoskeleton affects vacuolar morphology and contributes to auxin-induced growth repression. (***A-G***) Control seedlings (DMSO) (***A*** and ***E***) compared to Latrunculin B (LatB; 500 nM; 6 hr) (***B*** and ***F***) and Jasplakinolide (JASP; 2.5 µM; 6 hr) (***C*** and ***G***) treated seedlings. (***D***) Vacuolar morphology (vac. morph. [µm2]) index after depolymerization (LatB) and stabilization (JASP) of the actin cytoskeleton (Lifeact-Venus). (***H-K***) Cell length changes in fully elongated root cells in the differentiation zone. Untreated (DMSO) (***H***) and auxin (NAA; 125 nM for 20 hr) (***I***) treated ***Col-0*** wild type seedlings show reduction in cell length which is abolished by Latrunculin B (LatB; 125 nM; 20hr) cotreatment (***J*** and ***K***). Data

represent means ± SEM (***n*** = 30 cells from six individual seedlings for ***D***. YFP-VAMP711 (orange) and FM4-64 (red) were used to highlight the vacuole, and propidium iodide (green) for labeling the cell wall. *p < 0.05, ***p < 0.001. Scale bar: ***A-G*** = 5 µm; ***H-K*** = 50 µm.

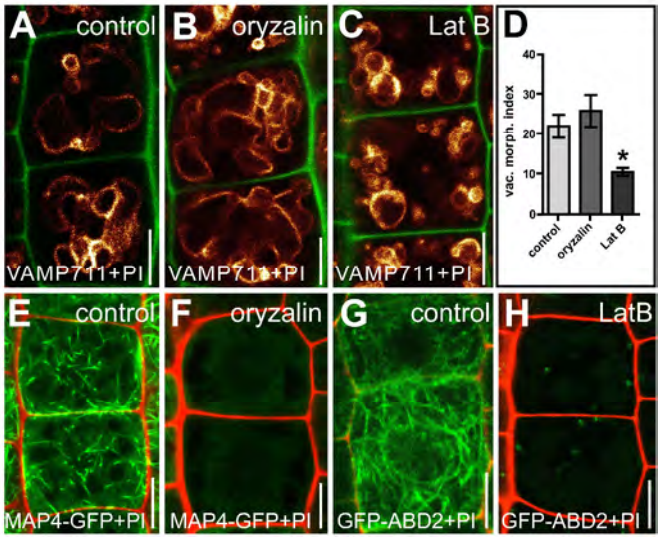

Fig. S4. Changes of vacuolar morphology upon interference with microtubules and actin. (***A-C***) DMSO solvent control (***A***), compared to the microtubule depolymerizing drug oryzalin (2 µM; 6h) treated (***B***) and latrunculin B (LatB; 500 nM; 6 hr) treated (***C***) seedlings. The vacuolar morphology (vac. morph. [µm2]) index was unchanged in oryzalin treated plants whereas LatB treated plants showed a significant decrease (***D***). The respective drug treatments in the presence of the microtubule marker MAP4-GFP (***E***) and the actin marker GFP-ABD2 (***G***) led to an almost complete loss of fluorescent signals (***F*** and ***H***), indicating that the used drug concentrations were sufficient to inhibit cytoskeleton formation. Data represent means ± SEM (***n*** = 25 cells from five individual seedlings for ***D***). (***A-C***) YFP-VAMP711 (orange) and propidium iodide (PI; green) were used to highlight the vacuole and the cell wall. (***E-H***) MAP4-GFP and GFP-ABD2 (green) were used to highlight microtubules and actin filaments, respectively. Propidium iodide to stain the cell wall is displayed in red (***E-H***). *p < 0.05. Scale bar: 5 µm.

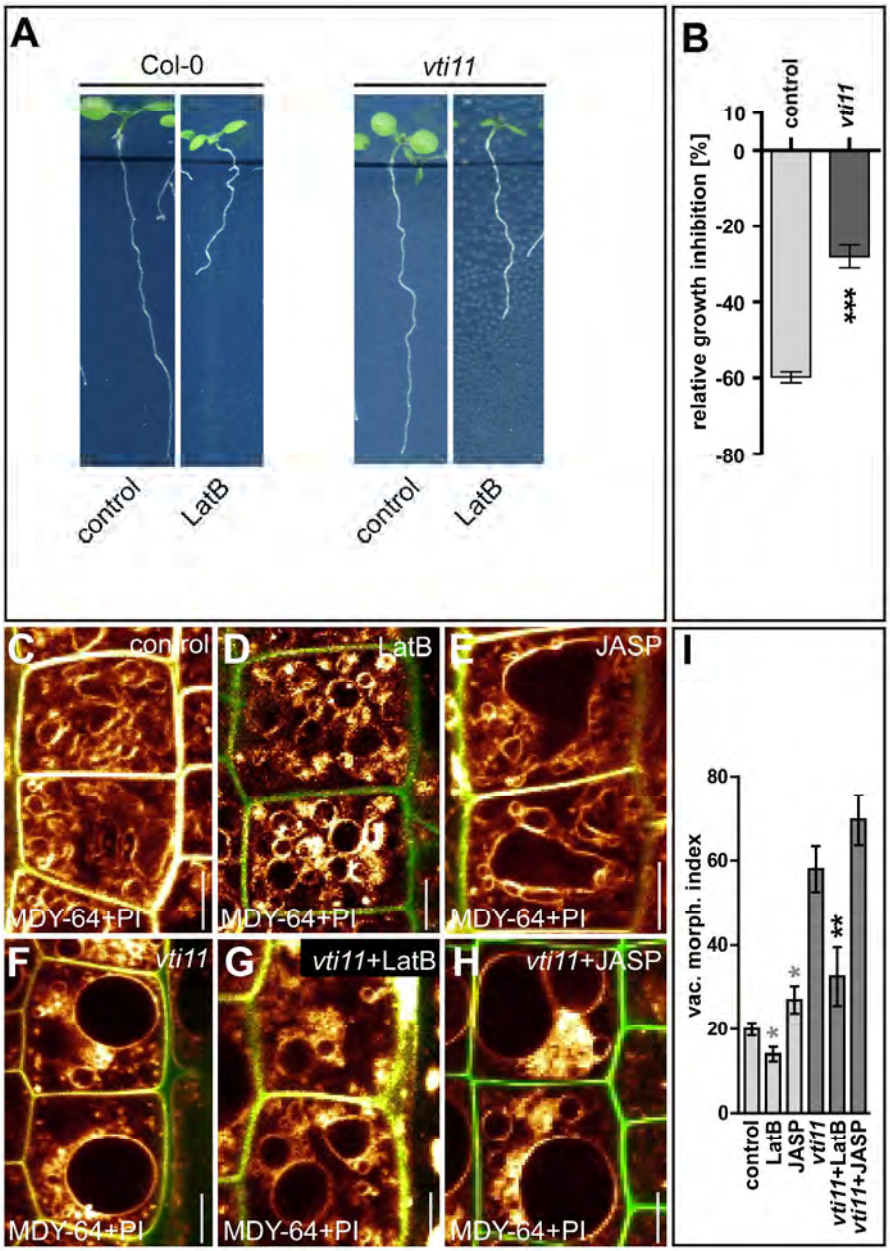

Fig. S5. Effect of actin interference on the SNARE mutant ***vti11***. (***A***) Root growth inhibition of Col-0 and ***vti11*** germinated on LatB (100 nM). Quantification of relative root growth inhibition (***B***). (***C-E***) Control seedlings (DMSO) (***C***) compared to latrunculin B (LatB; 500 nM; 6 hr) (***D***) and jasplakinolide (JASP; 2.5 µM; 6 hr) treated (***E***) seedlings. (***F-G***) Respective treatments, using the SNARE mutant ***vti11*** which displays significantly larger vacuoles (***F***), led to an imposed response to LatB (***G***) and a reduced response to JASP (***H***) treatments. All treatments were quantified, using the vacuolar morphology (vac. morph. [µm2]) index (***I***). Note: ***vti11*** vacuoles were significantly larger when compared to wild type ($p<0,001$). The LatB treated

vti11 mutant still displays larger vacuoles than wild type seedlings without LatB (compare ***C*** and ***G***). The MDY-64 stain (orange) and propidium iodide (PI; green) were used to highlight the vacuole and the cell wall, respectively. Data represent means ± SEM (n = 15-20 roots per condition for ***B and n*** = 30 cells from six individual seedlings for ***I***). Grey asterisks in ***I*** indicate statistical evaluation based on the control, black asterisks based on the ***vti11*** mutant. *$p < 0.05$, **$p < 0.01$, ***$p < 0.001$. Scale bar: 5 µm.

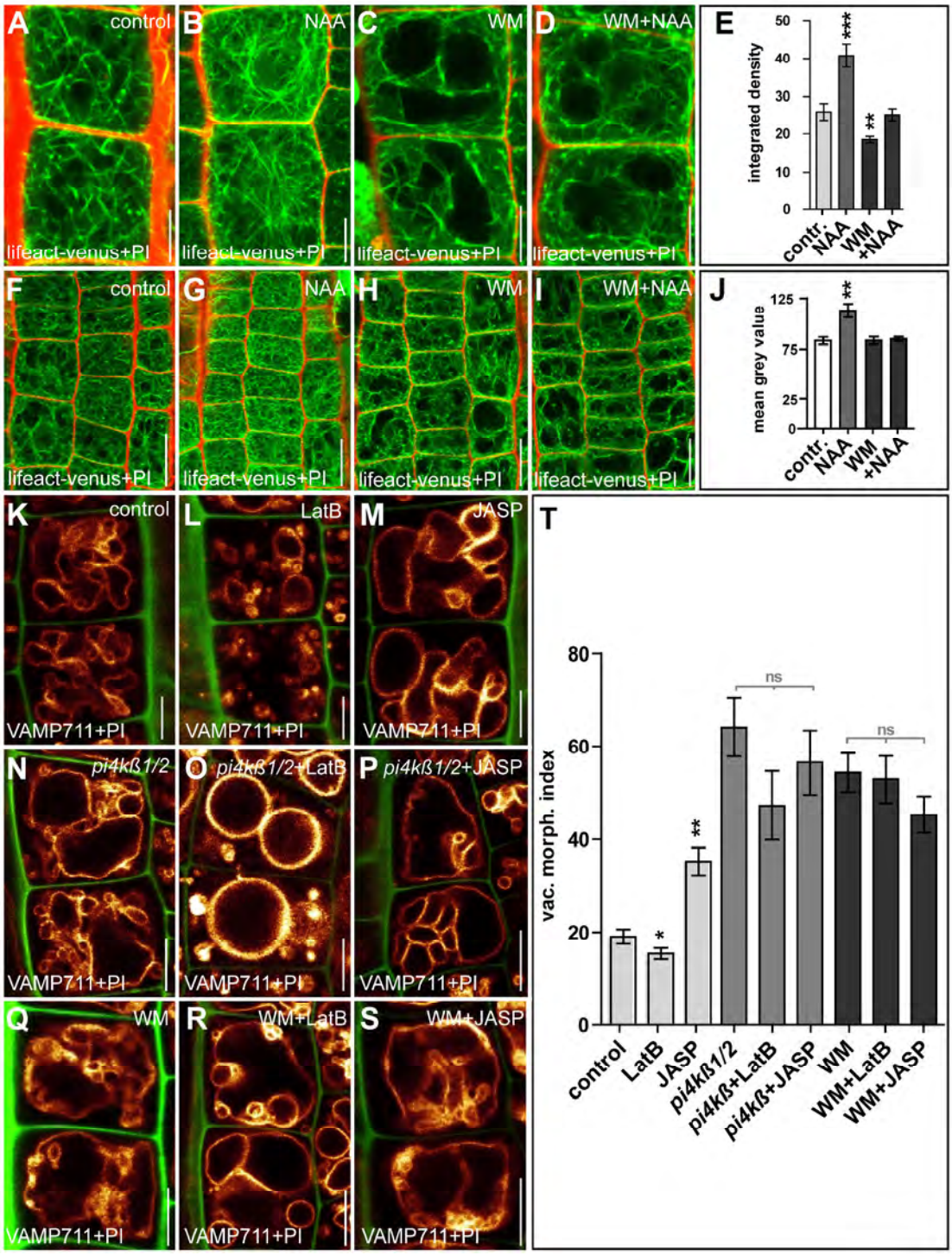

Fig. S6. Genetic and pharmacological interference with phosphatidylinositols partly abolishes auxin-induced changes on the cytoskeleton and the vacuolar morphology. (***A-D***) Control seedlings (DMSO) (***A***) compared to auxin (NAA; 500 nM; 6 hr) treated (***B***), wortmannin (WM; 33 µM; 6 hr) treated (***C***) as well as WM and NAA co-treated (***D***) seedlings. (***E***) Quantification of the integrated density of actin filaments (Lifeact-Venus). (***F-I***) Respective treatments were used to determine the signal intensity of Lifeact-Venus. Compared to the DMSO control (***F***) only NAA (***G***) treated, but not

WM (***H***) treated or WM and NAA co-treated (***I***) seedlings showed a significant change (***J***). (***K-M***) Vacuolar morphology changes upon genetic and pharmacological interference with phosphatidylinositols. Control seedlings (DMSO) (***K***) compared to latrunculin B (LatB; 500 nM; 6 hr) (***L***) and jasplakinolide (JASP; 2.5 µM; 6 hr) treated (***M***) seedlings. (***N-P***) Respective treatments, using the phosphatidylinositol kinase mutant ***pi4kß1/2*** (***N***) led to a strongly reduced response to LatB (***O***) and JASP (***P***) treatments. Co-treatments with the phosphatidylinositol kinase inhibitor WM (***Q***) also led to a reduced response to LatB (***R***) and JASP (***S***) treatments. All treatments were quantified, using the vacuolar morphology (vac. morph. [µm2]) index (***T***). Note: ***pi4kß1/2*** vacuoles and vacuoles after WM treatment were significantly larger when compared to wt ($p<0,001$). LatB treatment in ***pi4kß1/2*** and in presence of WM caused changes in vacuolar shape, displaying more roundish vacuoles (compare ***N*** to ***O***, ***Q*** to ***R***). Data represent means ± SEM (***n*** = 35-70 cells from 6-10 individual seedlings for ***E*** and ***n*** = 75 meristematic cells from five individual seedlings for ***J; n*** = 30 cells from six individual seedlings for ***T***). (***A-I***) Lifeact-Venus (green) and propidium iodide (PI; red) were used to highlight actin filaments and the cell wall, respectively. (***K-S***) YFP-VAMP711 (orange) and propidium iodide (green) were used to highlight the vacuole and the cell wall. Light grey bars in ***T*** indicate statistical evaluation within the ***pi14ß1/2*** mutant and within WM treatment. *$p < 0.05$, **$p < 0.01$, ***$p < 0.001$. Scale bar: ***A-D*** and ***K-S*** = 5 µm, ***F-I*** = 15 µm.

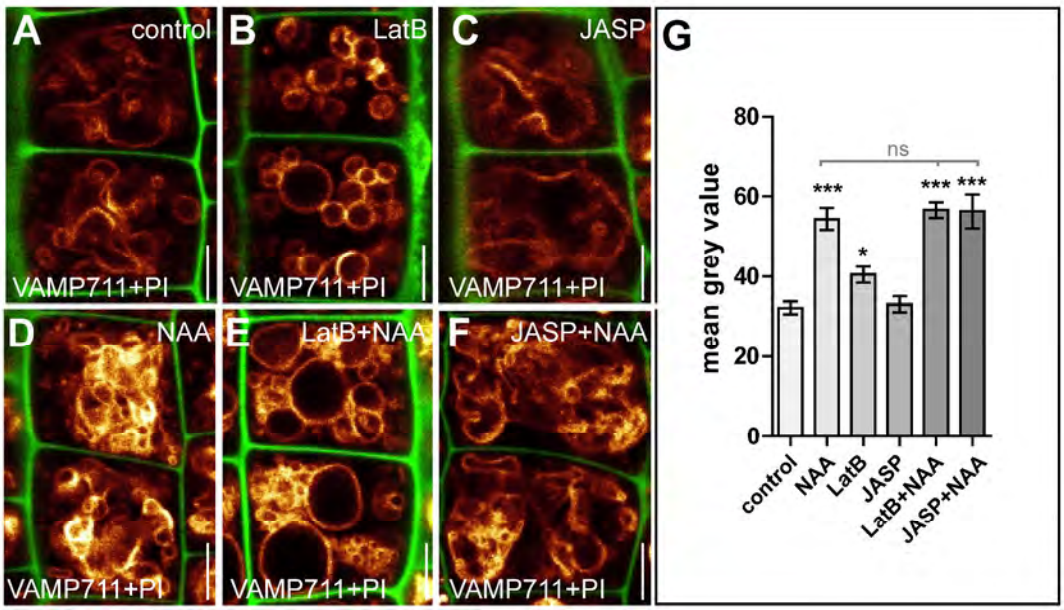

Fig. S7. Effect of actin interference on auxin-induced SNARE stabilization. (***A-C***) Control seedlings (DMSO) (***A***) compared to latrunculin B (LatB; 500 nM; 6 hr) (***B***) and jasplakinolide (JASP; 2.5 µM; 6 hr) treated (***C***) seedlings. (***D-F***) The auxin-induced (NAA; 500 nM; 6 hr) (***D***) increase in SNARE abundance was not affected by LatB (***E***) and JASP (***F***) co-treatments (***G***). Data represent means ± SEM (***n*** = 30 cells from six individual seedlings for ***G***). YFP-VAMP711 (orange) and propidium iodide (PI; green) were used to highlight the vacuole and the cell wall, respectively. Light grey bar indicates statistical evaluation of NAA treatment compared to NAA and LatB or NAA and JASP co-treatments. ns = not significant. *$p < 0.05$, **$p < 0.01$, ***$p < 0.001$. Scale bar: 5 µm.

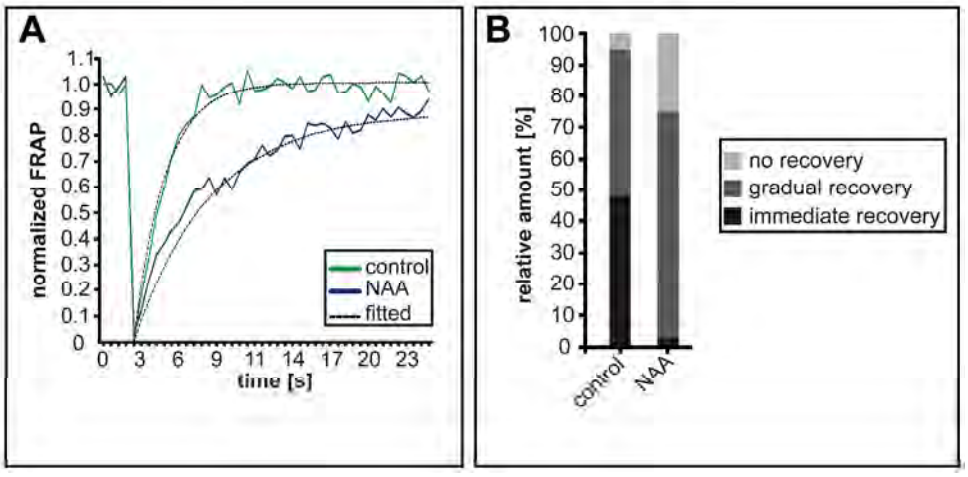

Fig. S8. Auxin treatments affect luminal vacuole dye diffusion. (***A*** and ***B***) Fluorescent Recovery After Photobleaching (FRAP) of BCECF-AM in control seedlings (DMSO) (***A***) compared to auxin (NAA; 250nM for 18 hr) (***B***) treated seedlings was measured. (***A***) Fluorescence recovery curves of BCECF-AM in auxin treated vacuolar structures show a slower recovery. (***B***) The amount of vacuoles recovering immediately was lower in auxin treated compared to untreated cells albeit the majority of signals were still able to recover. Graph in ***B*** represents measurements of ***n*** = 106 bleached structures for the control and ***n*** = 142 bleached vacuolar structures for NAA treatment.

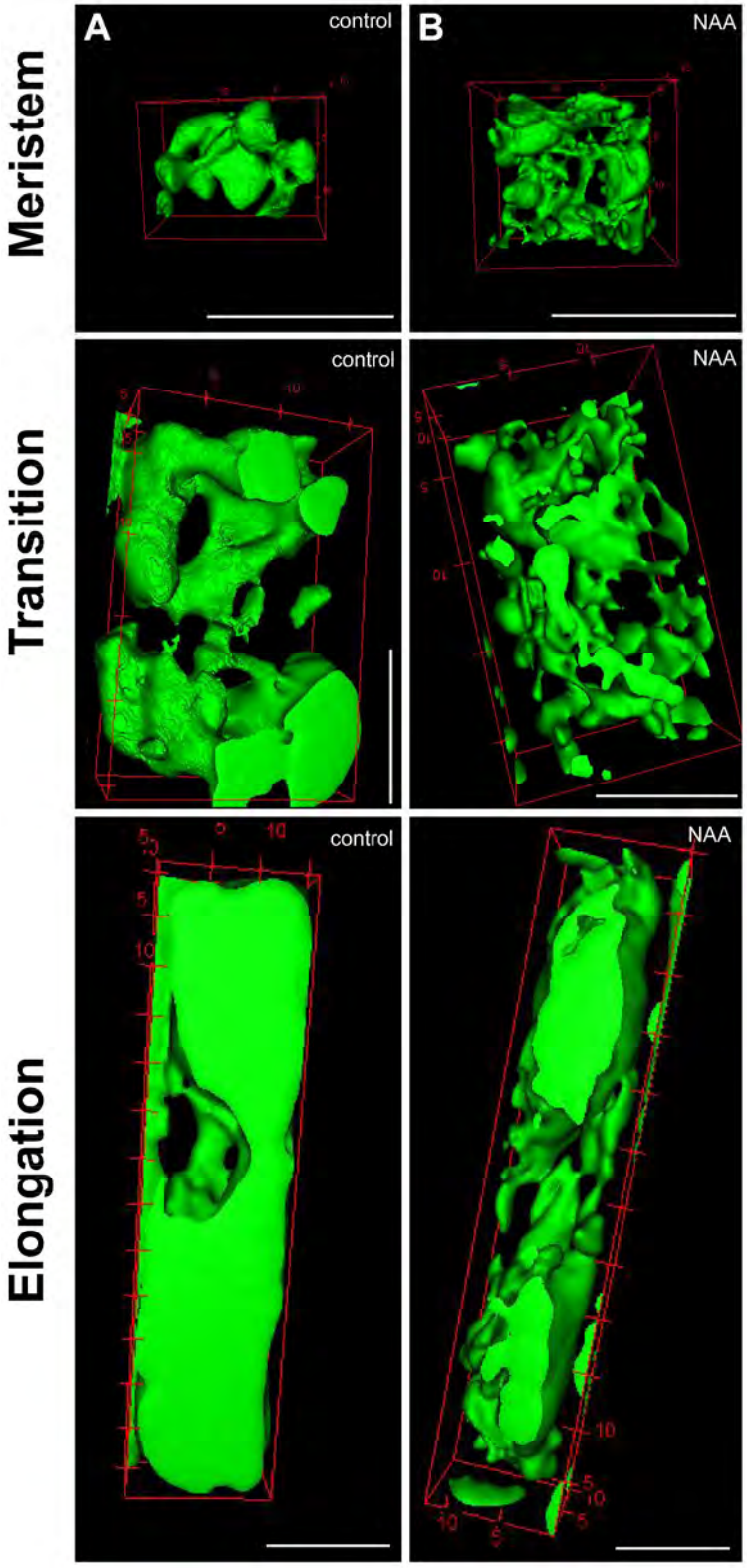

Fig. S9. Auxin effect on vacuolar morphology in the meristematic, transition and the early elongation zone. (***A*** and ***B***) Vacuole surface rendering of control seedlings (DMSO) (***A***) compared to auxin (NAA; 250 nM for 20 hr) (***B***) treated seedlings stained with BCECF-AM. The rendering was carried out for vacuoles in the meristem, the transition zone and the early elongation zone. Scale bar = 10 µm.

Movie S1. Vacuolar structures in the meristem are interconnected. 3D vacuole reconstruction of micrographs recorded by scanning electron microscopy, using Amira software.

Movie S2. Auxin treatment leads to constricted but not fragmented vacuoles. 3D vacuole reconstruction after auxin treatment (250 nM NAA, 20 hr) of micrographs recorded by scanning electron microscopy, using the Amira software.

Movie S3. Live cell imaging show that vacuolar structures are interconnected. 3D vacuole reconstruction of meristematic vacuoles stained by the luminal dye BCECF-AM and propidium iodide (cell wall).

Movie S4. Live cell imaging of auxin treated vacuoles show multiple constrictions. 3D vacuole reconstruction of meristematic vacuoles stained by the luminal dye BCECF-AM and propidium iodide (cell wall) after auxin treatment (250 nM NAA, 20 hr).